Preparation and property–performance relationships in samarium-doped ceria nanopowders for solid oxide fuel cell electrolytes

Marcin R. Kosinski, Richard T. Baker*

School of Chemistry, University of St Andrews, North Haugh, St Andrews, KY16 9ST, United Kingdom

ARTICLE INFO

ABSTRACT

In a systematic study, Samarium doped ceria (SDC) nanopowders, $Sm_xCe_{1-x}O_{2-x/2}$ ($x = 0.1$, 0.2 or 0.3), were prepared by a low temperature citrate complexation route. The synthesis and crystallisation of the SDC powders were followed by thermochemical techniques (TGA/DTA), X-ray diffraction, elemental analysis, specific surface area determination (BET) and electron microscopy (SEM and TEM). Mean crystallite sizes were found to be around 10 nm for all compositions calcined at 500 °C. Dense electrolyte bodies were prepared at 1300 °C, 1400 °C and 1450 °C using two sintering times, 4 h or 6 h. Densities of 91–97% of theoretical were obtained, with a marked improvement in density on going from 1300 °C to higher sintering temperatures. Grain size analysis was conducted using SEM. Grain size distributions were related to %Sm and sintering conditions. Impedance spectroscopy was used to determine the total, bulk and grain boundary conductivities, the related activation energies and enthalpies of defect association and ion migration. Sintering at 1400 °C/6 h or 1450 °C/4 h gave superior grain structure and conductivity, with oversintering occurring after more severe treatments. At 600 °C the highest total ionic conductivity was 1.81×10^{-2} S cm^{-1} for $Sm_{0.2}Ce_{0.8}O_{1.9}$. The relationships between chemical composition, sintering parameters, grain structure and electrochemical performance are discussed.

1. Introduction

Solid Oxide Fuel Cells (SOFCs) are widely accepted as a promising clean and efficient energy conversion technology. However, their relatively high temperature of operation and the presence of an oxidizing atmosphere at the air side and a strongly reducing atmosphere at the fuel side of the cell make the selection of materials for individual components of SOFCs very challenging. The electrolyte, apart from having excellent ionic conductivity, must meet certain criteria such as gas-tightness, chemical stability, thermal shock resistance and thermal expansion compatibility with electrodes and interconnect materials. Currently, several ionically conducting ceramics are employed as SOFC electrolytes. The most effective of these are based on allovalently substituted zirconium and cerium oxides. The most important dopants are Y^{3+}, Sc^{3+} and Ca^{2+} in ZrO_2 and Gd^{3+} and Sm^{3+} in CeO_2 [1–4].

Sm-doped ceria (SDC) and Gd-doped ceria (GDC) possess higher ionic conductivity than yttria-stabilised zirconia (YSZ) when compared at the same temperature. However, GDC and SDC are less redox stable than YSZ and begin to show significant electronic conductivity because of the variable oxidation state of Ce at higher temperatures, especially under reducing conditions. This complicates the application of these materials as electrolytes in high-temperature SOFCs, which operate typically at 800–1000 °C. However, ceria-based ceramics are proposed as promising electrolytes for intermediate-temperature SOFCs (IT-SOFCs), working at around 500–700 °C. Ceria and doped ceria materials are used in other high-temperature applications, such as three-way automotive catalysts, gas sensors and ceramic oxygen generators, where their electronic conductivity is less problematic and even advantageous [5–7]. They are also of considerable interest for use as anode materials, especially for IT-SOFCs running on hydrocarbon fuels in which carbon deposition – which deactivates other anodes such as Ni-YSZ – is much reduced in extent and less deactivating [8–10].

The ionic conductivity of an electrolyte strongly depends on the concentration, formal charge and ionic radius of the dopant cations. Partial substitution of Zr^{4+} or Ce^{4+} by di- or trivalent cations produces oxygen vacancies in order to maintain the charge neutrality of the crystal lattice. Thus, ionic transport in the fuel cell electrolyte becomes possible by the movement of oxygen ions via these vacancies down the chemical potential gradient caused by the large difference in O_2 partial pressure between the anode and cathode of the fuel cell. The conductivity enhancement in doped ceria electrolytes caused by the oxygen vacancies introduced in this way has been investigated by several researchers. Mogensen et al. pointed out the concept of the matching radius, which is based on minimal difference between the host Ce^{4+} and dopant cation [11]. Kilner suggested that the increase in ionic conductivity is a
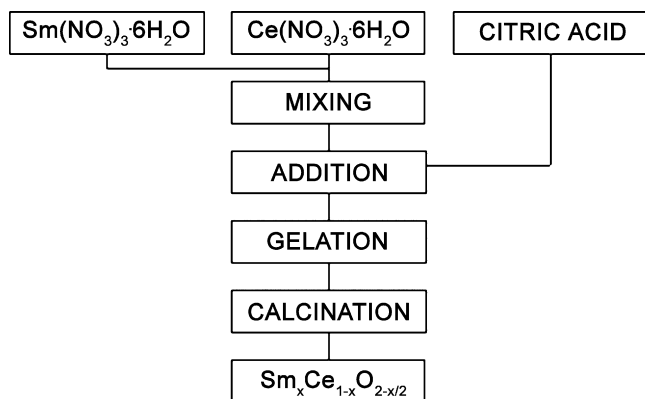
Fig. 1. Experimental flow chart for the synthesis of SDC powders.

result of the small association enthalpy between the dopant cation and the associated oxygen vacancies in the fluorite lattice [12]. On the other hand, other researchers report that other key factors are the synthesis method employed and the particle size of the powders used in the formation by sintering of the dense electrolyte. These powders can be synthesized by a variety of techniques such as conventional powder mixing and calcination, co-precipitation, sol–gel and other combustion routes [13–16]. Among them, the solution methods are recognized to be relatively simple to perform, inexpensive and effective for producing high specific surface area powders with ultra-fine particle sizes.

In this work, we present a systematic study of SDC solid solutions of three compositions obtained using a low temperature citrate complexation method. This simple method yields high purity nanoparticulate powders which are of interest for obtaining good electrolyte densities at relatively low sintering temperatures without any sintering promoters. In this contribution, the initial synthesis of the materials was studied by thermochemical and XRD methods and the resulting powders were characterised structurally and chemically. Electrolytes were prepared from these nanopowders under six different sintering regimes and the grain structure of the resulting SDC ceramics was studied and related to their ionic conductivity, as determined by impedance spectroscopy.

2. Experimental

Three compositions of $Sm_xCe_{1-x}O_{2-x/2}$ were prepared with $x = 0.1, 0.2$ and 0.3 and these were named 10SDC, 20SDC and 30SDC, respectively. Similar procedures were used to those developed for the preparation and study of GDC [17,18]. Stoichiometric amounts of metal nitrate hexahydrates, $Ce(NO_3)_3·6H_2O$ and $Sm(NO_3)_3·6H_2O$ (Acros Organics, 99.5%), were dissolved in deionized water separately to make 0.1 M solutions. These were stirred to homogenise and combined. Anhydrous citric acid (Alfa Aesar, 99.5%) was dissolved in water (0.2 M) and this solution was added to the cation solution in the ratio of two moles citrate per mole of total metal cations. After homogenization of the solution, the temperature was increased to 80 °C and maintained under stirring for 12 h. Simultaneous elimination of water and gas caused an increase in the viscosity of the mixture. The resulting gel became transparent, then increasingly viscous with formation of yellow foam and dark brown bubbles. The initial thermal decomposition of the gel was carried out in a muffle furnace at 250 °C for 2 h. The resulting, ash-like materials were calcined in static air in a tube furnace at 500 °C for 2 h. In both steps, heating and cooling rates were 2.5 °C min^{-1} and 5 °C min^{-1}, respectively. Fig. 1 illustrates the procedure of the citrate complexation method employed in this work. After calcination, each powder was placed in 50 cm^3 Nylon jars and dry ground for

1 h using a planetary ball mill (Fritsch Pulverisette 7) operated at 400 rpm. Zirconia balls of 10 mm diameter were used as the grinding medium with a ball to powder weight ratio of 10:1. The milling process was interrupted every 15 min to dislodge the powder from the walls of the container. The three resulting nanopowder compositions were characterised in detail and were used to make the sintered electrolyte pellets.

The thermal behaviour of the precursor gels was investigated by thermogravimetric analysis (TGA) and differential thermal analysis (DTA) using a Netzsch STA 449C Jupiter instrument. The heat flow and weight change of samples placed in Pt crucibles were measured in air (50 ml min^{-1}) from 25 °C to 800 °C at a heating rate of 5 °C min^{-1}. In addition, these experiments were repeated in flowing oxygen to allow simultaneous analysis of off-gases by mass spectrometry (MS).

The crystal structure of the specimens was analyzed by XRD using a Philips diffractometer (PW 1710) operated at 40 kV and 40 mA with CuK$_\alpha$ monochromatic radiation. High-grade silicon powder was used as an external standard to allow correction for instrumental broadening. Data acquisition was performed at room temperature by scanning 2θ from 10° to 100° with a step length of 0.02° and at a rate of 1° min^{-1}. XRD patterns were fitted using Rietveld procedures in the FullProf programme [19].

The values of residual carbon content were investigated for samples calcined for 2 h at temperatures from 250 °C to 900 °C using a Carlo Erba 1110 CHNS analyser. Brunauer–Emmett–Teller analysis (BET) by nitrogen adsorption were performed on the nanopowders using a Micrometrics ASAP 2020 instrument in order to obtain values of specific surface area (SSA). All samples were pretreated at 120 °C for 6 h.

The SDC nanopowders were analyzed by means of electron microscopy. Transmission Electron Microscopy (TEM) images were obtained using a JEOL JEM-2011 HRTEM instrument. The sample was prepared by dipping 3 mm Cu grids coated with holey carbon film into an ultrasonicated dispersion of SDC powder in hexane and allowing this to dry overnight. Chemical analysis was performed in the TEM by Energy Dispersive X-ray Spectroscopy (EDX). Scanning Electron Microscopy (SEM) images were obtained using a Philips XL30 ESEM instrument equipped with a field emission gun. Samples were coated with 30 nm of Au/Pd to reduce charging.

The sintering properties of compressed samples were studied using a Netzsch DIL 402C dilatometer. The powders calcined at 500 °C for 2 h were uniaxially pressed at 200 MPa in a 10 mm diameter die. After performing a correction run with an alumina specimen, SDC samples were subjected to a temperature programme which consisted of heating from ambient to 1470 °C at a rate of 2 °C min^{-1} followed by an isothermal dwell at 1470 °C for 6 h. Air (50 ml min^{-1}) was employed as the purge gas.

Dense electrolyte pellets were prepared from the nanopowders calcined at 500 °C for 2 h by uniaxial pressing at 200 MPa in a 13 mm diameter cylindrical die and firing in static air under six different sintering regimes. Sintering temperatures of 1300 °C, 1400 °C and 1450 °C were applied, each for either 4 h or 6 h. Heating and cooling rates were 2 °C min^{-1} and 4 °C min^{-1}, respectively. These pellets were polished and thermally etched for examination using SEM. The etching process was carried out at a temperature 50 °C lower than the corresponding sintering temperature, employing a short dwell time of 1 min but identical ramp rates. Pellets were coated with a 15 nm layer of Au-Pd and SEM images were obtained using a JEOL JSM-5600 instrument. Statistical grain size analyses were carried out for each sample using these images.

The nanopowders calcined at 500 °C for 2 h were also used to prepare symmetrical cells for two-electrode conductivity measurements by Impedance Spectroscopy (Solartron 1260 FRA). The electrolytes were made by uniaxially pressing the powders at 200 MPa in a 25 mm diameter cylindrical die and sintering using

identical conditions and ramp rates to those used for the SEM studies. After polishing, Pt ink (inorganic-free, Engelhardt) was used to deposit electrodes on both sides of the pellet using a screen printer. Electrical connections were made by attachment of Pt wire (Alfa Aesar, 0.25 mm dia, 99.9%) and by firing the electrodes at 1000 °C for 1 h. The resulting pellets were placed in a quartz reactor and this was placed in a tube furnace. Complex impedance measurements were carried out under an atmosphere of flowing pre-dried, synthetic air (50 ml min^{-1}) at a number of temperatures over the range 150–800 °C. An a.c. voltage of 0.1 V amplitude was applied and the frequency was swept from 20 MHz to 1 Hz. At each test temperature, spectra were recorded repeatedly until no change was noted between them. Spectra were analysed and fitted using the ZView software (Scribner Associates, Inc.).

3. Results and discussion

3.1. Nanopowder synthesis

Plots of TGA/DTA experiments performed in air on gel precursors of all three sample compositions are presented in Fig. 2. In each case, total weight loss was about 67% and occurred in three main steps in the approximate mass ratio 3:1:2 with increasing temperature. Each of these steps corresponded to a peak representing an exothermic process in the DTA trace. At temperatures higher than 500 °C the TGA curve showed no change, implying that no further mass loss occurred. The peak positions, p_n, and associated enthalpy changes, ΔH_n, of the three exothermic peaks ($n = 1$–3) are presented in Table 1. ΔH values were calculated by integrating the associated peak in the DTA graph, calibrating for the final sample mass and expressing the result per mole of final product. Some care is necessary in the interpretation of these values but they are of some use, in conjunction with the other thermochemical results, in assigning chemical processes to the three exothermic peaks. The DTA traces of all three precursor gels exhibited two large (p_1 and p_3) and one small exothermic peak (p_2). These were shifted towards higher temperatures with increasing Sm content. In addition, one small endothermic peak (p_0) was seen at ~107 °C for all samples and can be assigned to the evaporation of physically adsorbed water. Apparent changes in heat flow in the form of drift and some sharp fluctuations were observed in all samples at temperatures from 400 °C to 800 °C. It is believed that these were instrumental artefacts. First derivative curves of the TGA and DTA data (not shown) showed no change in this temperature range.

The TGA/DTA experiments were repeated for all three precursor gels in a flow of pure oxygen. A representative example (for 30SDC) is presented in Fig. 2(d). Analysis of off-gases was carried out using a quadrupole mass spectrometer. Pure O_2 was used to avoid masking CO and N_2 (both mass/charge ratio, $m/q = 28$) released by the sample with the large concentration of N_2 in air. It was found that H_2O ($m/q = 18$) was the main product liberated in the first peak – starting at ~110 °C with its maximum at 126 °C – together with large amounts of CO and CO_2 (28, 44) and small amounts of NO and NO_2 (30, 46). The associated ΔH_1 value was around −100 kJ mol^{-1}, depending on sample composition. This peak is thought to relate to the polymerization reactions accompanying the completion of gel formation. The presence of the second exothermic peak – at 175–230 °C – was also reflected in the MS data. Here, small peaks could be assigned to release of CO, CO_2 and H_2O with a small amount of NO and negligible NO_2. The matching peaks in the C trace ($m/q = 12$) confirmed the CO_2 and CO peaks. This peak can be assigned to breakdown of the citrate species by dehydration and loss of carboxylate groups as CO_2. The temperature at which this peak occurs matches well with the decomposition temperature of citric acid, 175 °C, [20] bearing in mind that this is a transient
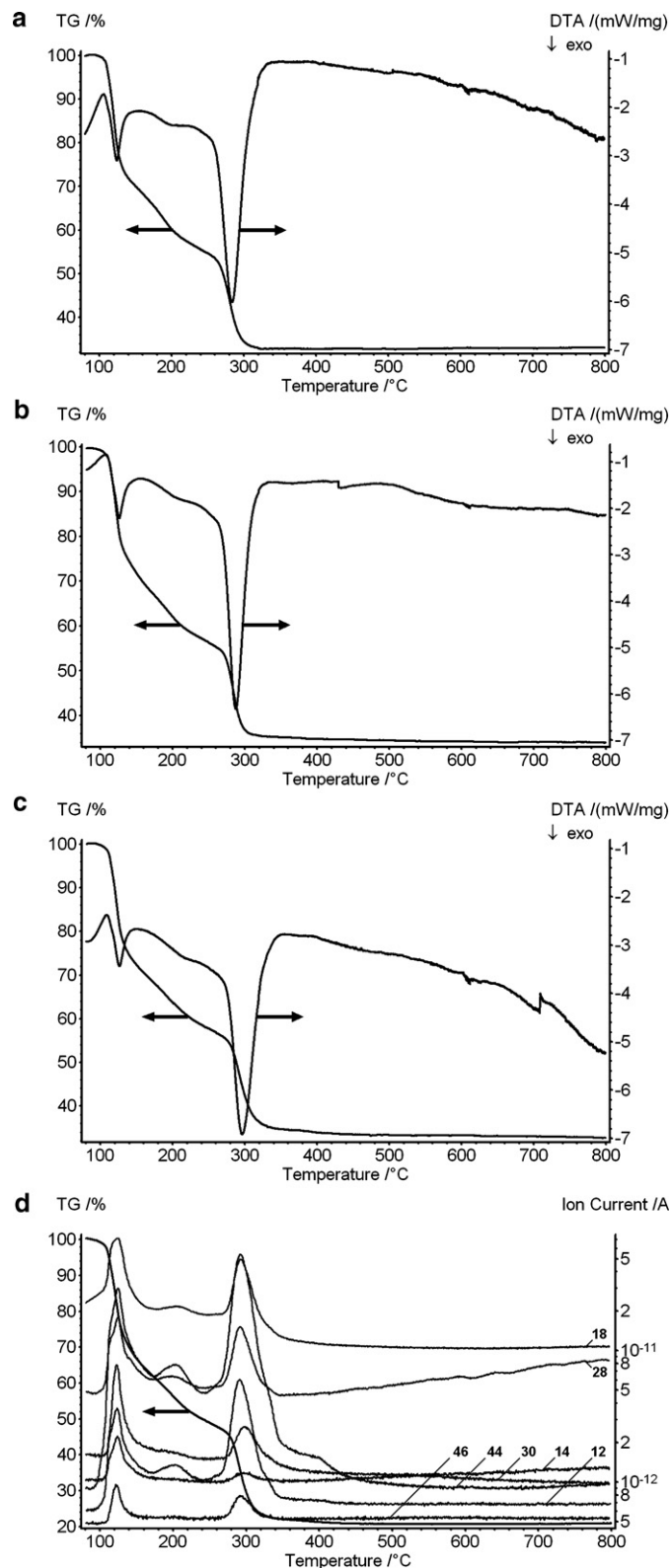

Fig. 2. Plots of TGA and DTA experiments run in air on precursor gels of (a) 10SDC, (b) 20SDC and (c) 30SDC. (d) TGA and DTA plots run in O_2 for 30SDC including mass spectrometry data. Mass to charge (m/q) ratios are indicated. Note the log scale for ion current.

Table 1
Summary of DTA plots for SDC gel precursors run in air.

Sample	$p_0/°C$	$p_1/°C$	ΔH_1[a]$/kJ\,mol^{-1}$	$p_2/°C$	ΔH_2[a]$/kJ\,mol^{-1}$	$p_3/°C$	ΔH_3[a]$/kJ\,mol^{-1}$
10SDC	107	125	−137	203	−11.7	284	−920
20SDC	109	126	−132	212	−8.63	288	−772
30SDC	107	127	−95.3	225	−18.0	297	−836

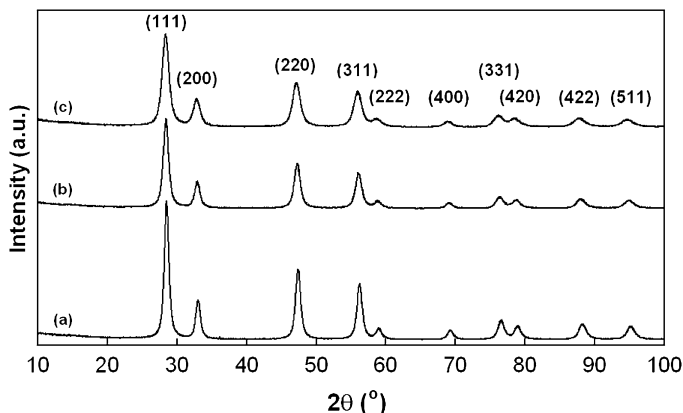[a] ΔH values expressed per mole of final product.

Fig. 3. XRD patterns of (a) 10SDC, (b) 20SDC and (c) 30SDC powders calcined at 500 °C for 2 h.

experiment and so processes will be shifted to slightly higher temperatures than would pertain at steady state. The small value of ΔH_2 supports the assignment of this peak as a decomposition rather than a combustion, which would be more exothermic. The third peak – starting at 265 °C – corresponded to the final release of large amounts of CO_2, CO and H_2O with only very small amounts of NO_x. This was attributed to the final complete burn out of the remaining organic matter to leave only oxide material. This assignment is supported by the large value of ΔH_3 – around −800 kJ mol^{-1} – which is consistent with an energetic combustion reaction. The NO_x peaks were generally small and decreased in size, relative to those for water and carbon oxides, as temperature increased in the TGA/DTA experiment. This indicates that most of the nitrogen was liberated during the gel formation step at 80 °C. This is confirmed by the observation of the evolution of large amounts of brown gas during this step.

Fig. 3 presents XRD patterns of the three SDC compositions calcined at 500 °C for 2 h. All peaks were assigned to the cubic fluorite crystal structure, typical of ceria powders. There was no evidence of any other phases. Small shifts of the diffraction peaks to lower 2θ were noticed as Sm content increased. This corresponded to a smooth expansion of the ceria unit cell dimension from 5.4229 Å to 5.4431 Å on going from 10SDC to 30SDC. The lattice parameters and the average crystallite size of the three SDC compositions are summarized in Table 2. The values presented are means of patterns obtained for six different batches of each composition for SDC samples calcined at 500 °C for 2 h. These results are consistent with crystallographic data from ICSD for these compositions. Average crystallite size (D_{XRD}) was calculated from the degree of line broadening in the main (1 1 1) diffraction peak using the Scherrer

equation (Eq. (1))

$$D_{XRD} = \frac{0.9 \cdot \lambda}{\beta \cdot \cos\theta} \tag{1}$$

λ is the wavelength of the X-rays (nm), θ is the diffraction angle, β is the corrected full width at half maximum (FWHM) intensity [where β_m is the measured FWHM intensity of the (1 1 1) reflection and β_s is the measured FHWM of the standard silicon sample, 0.15°)].

Average crystallite size decreased as Sm content increased, the smallest value being 7.8 nm for 30SDC. Therefore, the XRD data confirmed that SDC nanopowders of ~10 nm mean crystallite size had been successfully prepared via the citrate complexation route followed by calcination at 500 °C for 2 h.

More detailed XRD studies were performed for the 10SDC composition after calcination at different temperatures for 2 h, starting with the precursor gel. As is seen in Fig. 4, diffraction patterns taken after treatment at 100 and 200 °C showed that the material was amorphous to the X-rays. After treatment at 300 °C, however, the expected diffraction pattern is clear, even though the peaks are very broad. Therefore, initial crystallization of the product must have taken place between 200 °C and 300 °C. This is consistent with thermal analysis data in which the final burn out of organics, which would leave only inorganic oxide material, peaked just below 300 °C. As treatment temperature increased further the peaks became gradually narrower, indicating increasing mean crystallite size with increasing temperature. The Scherrer equation (Eq. (1)) was again used to obtain values for mean crystal size and these are presented in Table 3. A qualitative analysis of all these XRD patterns indicated only reflections relevant to the cubic phase of samarium-doped ceria.

Elemental analysis was performed to obtain values for carbon content in the three SDC compositions after calcination at temperatures from 250 °C to 900 °C. The data are presented in Table 4 and show that carbon content was low even after calcination at just 250 °C and that it fell to very low values after calcination at 500 °C. The amount of residual carbon at 500 °C was considered to have negligible impact on these materials and this calcination treatment was employed for further studies on the SDC solid solutions. Carbon
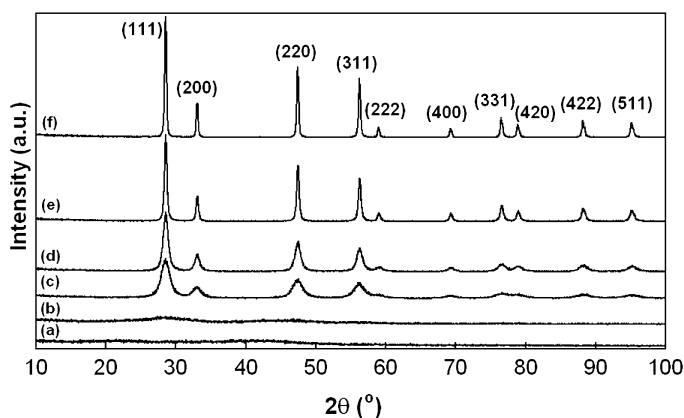
Table 2
Lattice parameters and average particle size for SDC powders calcined at 500 °C for 2 h.

Sample	ICDD	$a_{th}/Å$	$a/Å$	$V/Å^3$	D_{XRD}/nm
10SDC	01-075-1757	5.4230	5.4229(4)	159.48(3)	11.3(4)
20SDC	01-075-1758	5.4330	5.4332(2)	160.38(1)	9.1(3)
30SDC	01-075-1759	5.4430	5.4431(4)	161.26(4)	7.8(5)

Fig. 4. XRD patterns of the 10SDC samples calcined for 2 h at (a) 100 °C, (b) 200 °C, (c) 300 °C, (d) 500 °C, (e) 700 °C and (f) 900 °C.

Table 3
Lattice parameters, volume of the unit cell and crystallite size of SDC powders calcined at different temperatures.

$T/°C$	10SDC			20SDC			30SDC		
	$a/Å$	$V/Å^3$	D_{XRD}/nm	$a/Å$	$V/Å^3$	D_{XRD}/nm	$a/Å$	$V/Å^3$	D_{XRD}/nm
250	5.4228	159.47	5.54	5.4329	160.36	4.83	5.4428	161.24	4.34
300	5.4229	159.48	5.87	5.4330	160.37	5.10	5.4434	161.29	4.77
500	5.4228	159.47	10.95	5.4328	160.35	9.23	5.4438	161.33	8.22
700	5.4229	159.48	25.15	5.4332	160.39	21.98	5.4435	161.30	19.51
900	5.4230	159.48	44.32	5.4335	160.41	40.92	5.4426	161.22	32.19

Table 4
Carbon content (wt%) in SDC powders calcined at different conditions.

$T/°C$	t/h	10SDC	20SDC	30SDC
250	2	0.85	0.96	1.51
300	2	0.45	0.62	1.01
500	2	0.19	0.23	0.44
700	2	0.07	0.08	0.19
900	2	0.03	0.04	0.09

content increased slightly with increasing Sm content.

As found in previous studies, the SSAs for doped ceria powders prepared by the citrate method could be significantly increased by subjecting them to a dry milling step [17]. Table 5 shows the values of SSA (A) of SDC powders calcined at different temperatures for 2 h and then milled using a planetary ball mill with zirconia balls at 400 rpm for 1 h. Values of A were converted to equivalent particle diameters (D_{BET}) using Eq. (2), assuming spherical particle shape. In Table 5, values of D_{BET} are compared with values of average crystallite size calculated from the XRD patterns (D_{XRD}) using the Scherrer equation (Eq. (1)).

$$D_{BET} = \frac{6 \times 10^3}{\rho_{XRD} \cdot A} \tag{2}$$

A is specific surface area ($m^2\,g^{-1}$) and ρ_{XRD} is the theoretical density calculated from crystallographic data ($g\,cm^{-3}$).

The SSA (A) of the SDC powders significantly decreased, and particle size, D_{BET}, correspondingly increased, as the calcination temperature increased, for all compositions. The highest values of SSA were found for 10SDC up to 500 °C. Above that temperature, 20SDC had the highest SSA until 900 °C, when the values for 10SDC and 20SDC were equal. The average particle size, D_{BET}, also showed a general tendency to increase with increasing Sm content at a particular calcination temperature, although there were exceptions to this at 500 °C and 700 °C. For any particular sample, the val-

Table 5
Specific surface area, A, and average particle size of SDC powders after different treatments.

$T/°C$	Sample	$A/m^2\,g^{-1}$	D_{BET}/nm	D_{XRD}/nm	D_{BET}/D_{XRD}
250	10SDC	58.8	14.2	5.5	2.6
	20SDC	57.6	14.6	4.8	3.0
	30SDC	45.4	18.6	4.3	4.3
300	10SDC	52.6	15.9	5.9	2.7
	20SDC	49.2	17.1	5.1	3.3
	30SDC	37.9	22.3	4.8	4.6
500	10SDC	30.2	27.7	10.9	2.5
	20SDC	32.7	25.7	9.2	2.8
	30SDC	21.8	38.7	8.2	4.7
700	10SDC	12.9	64.8	25.2	2.6
	20SDC	15.5	54.2	22.0	2.5
	30SDC	10.2	82.7	19.5	4.2
900	10SDC	7.0	119.4	44.3	2.7
	20SDC	7.0	120.0	40.9	2.9
	30SDC	6.3	133.8	32.2	4.2

ues of average particle size, D_{BET}, and average crystallite size, D_{XRD}, were not in agreement, even at low temperatures. This disagreement could be caused by the occurrence of crystalline nanodomains within individual nanocrystals. These nanodomains would register in XRD as individual crystals while the BET technique would measure the surface area of the parent nanocrystal only. Highly defective crystals may also give rise to line-broadening in XRD. However, another explanation is that the nanocrystals clustered together to form agglomerates of crystalline nanoparticles. If this is the explanation, the D_{BET}/D_{XRD} ratio is an index of extent of agglomeration. Curiously, these ratios appeared to be independent of temperature, even though the SSA and particle sizes were changing considerably. For each calcination temperature, therefore, the relationship between this ratio for the three compositions is essentially the same. Values for 10SDC and 20SDC are very similar while that for 30SDC is clearly higher.

Electron microscopy was used to study the morphology of the SDC nanopowders. Fig. 5 shows the microstructure of as-calcined powders before milling. Sponge-like, shell-like and branched structures were observed for all compositions after calcination at 500 °C for 2 h. The highly porous morphology of this as-prepared material is very likely to be caused by the large volumes of gas produced in the preparation method which have been discussed above in connection with the thermochemical analysis of the synthesis step. Equally, the presence of very small pores and their wide distribution is likely to relate to the intimate mixing of reactants achieved in the citrate complexation method. On the macroscale, these powders consisted of papery, fragile structures and were very voluminous. To break down the material, release the nanoparticles and increase the SSA, the materials were milled at 400 rpm for 1 h. Fig. 6 presents SEM images of the resulting milled SDC nanopowders. All three compositions appeared to consist of open structures of roughly spherical clusters made up of a relatively small number of clearly distinguishable primary particles. The spherical shape of these clusters may be advantageous in the preparation of dense pellets in the sintering step. The observation of clustering of the primary particles would tend to support the assignment of the D_{BET}/D_{XRD} ratio as an index of agglomeration.

TEM images of all SDC powder samples at low, medium and high magnification are shown in Fig. 7. All compositions consisted of loosely agglomerated sheets and clusters which were composed of individual crystallites of diameter ~10 nm. The internal crystal structure of individual nanoparticles was observed using high resolution (HR) TEM. These crystallites showed good crystallinity and there was no evidence for widespread defective crystal structures or for crystallites containing several nanodomains. In the absence of these phenomena, therefore, the TEM data confirmed the validity of using the ratio D_{BET}/D_{XRD} as an index of agglomeration. Digital Diffraction Patterns (DDPs) were obtained by processing specific areas of HRTEM images using a Fast Fourier Transform routine. Examples are inset in the corresponding images in Fig. 7(C), (F) and (I). These represent three different crystallographic orientations and were indexed to the fluorite structure viewed in the [0 0 1], [0 1 1] and [1 1 2] zone axes, respectively. These patterns, and the interplanar spacings measured from them, were consis-
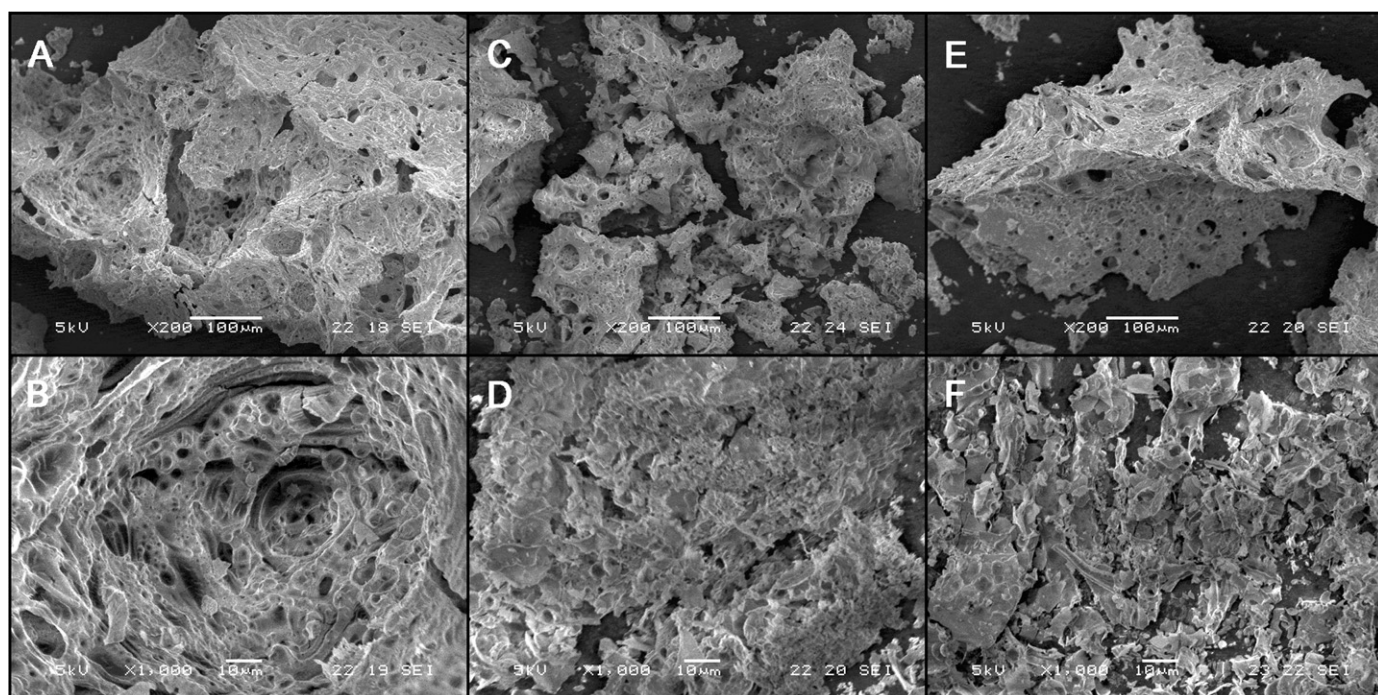
Fig. 5. Low and high magnification SEM images of unmilled SDC powders calcined at 500 °C for 2 h. (A, B) 10SDC; (C, D) 20SDC; (E, F) 30SDC.

tent with substituted ceria. EDX analysis was performed in the TEM on several areas of each sample after calcination at 500 °C and confirmed x in $Sm_xCe_{1-x}O_{2-x/2}$ to be 0.094 ± 0.004, 0.202 ± 0.004 and 0.300 ± 0.002 (errors are two standard deviations) for 10SDC, 20SDC and 30SDC, respectively.

3.2. Sintering step and pellet characterisation

Dilatometry experiments were performed on compacted green pellets of each of the 10SDC, 20SDC and 30SDC nanopowder compositions to investigate the sintering properties of the powders. Fig. 8 presents the % change in length, dL/L_o, for each sample and the temperature profile applied. For all three samples, a total dimensional change of 16–18% took place. All three curves had broadly similar shapes. In all cases the sintering, or compaction, process started gradually at temperatures as low as 200 °C but the shrinkage process was relatively slow up to about 500 °C. This is logical since the powders had already been calcined at 500 °C for 2 h during their preparation. From 500 °C to 600 °C, sample volume decreased rapidly, for 10SDC at an approximately constant rate but for 20SDC and 30SDC in what appeared to be a two-stage process with the higher rates at the higher temperatures. Sintering of the 10SDC was essentially complete by about 1350 °C. However, for the 20SDC and 30SDC, some sintering clearly continued – although at a low rate – after the samples had reached the maximum temperature of 1470 °C. After 6 h at 1470 °C sintering in all samples did appear to be essentially complete since the rate of dimensional change was negligible by this point.

The dilatometry results were used to set the conditions of the six sintering regimes to be used in further study of the microstructure and conductivity of the sintered SDC pellets. Three temperatures spanning the range over which sintering finished its rapid phase – 1300 °C, 1400 °C and 1450 °C – and two sintering times – 4 and 6 h – were applied to each of the three SDC compositions. This gave a total of 18 distinct pellet samples. XRD studies on the SDC pellets sintered at 1450 °C for 6 h – the most severe conditions – were consistent with a single phase of fluorite structure. Fig. 9 shows XRD patterns of the three SDC compositions. These contained no

evidence of impurity peaks and since the nanopowders after calcination at 500 °C also appeared to be phase-pure (Fig. 3), it can reasonably be assumed that the five less severe sintering regimes also gave rise to high purity pellets. The peaks in Fig. 9 are much sharper than those presented in Fig. 3 for the nanopowders, because of the significant growth in particle size during sintering.

The theoretical densities of the SDC crystal structures were calculated according to Eq. (3) from the crystallographic information obtained by XRD.

$$\rho_{XRD} = \frac{4 \cdot [(1-x) \cdot M_{Ce} + x \cdot M_{Sm} + (2 - (x/2)) \cdot M_O]}{a^3 \cdot N_{Av}} \quad (3)$$

M is atomic weight (g mol^{-1}), x is the dopant mole fraction, a is the unit cell lattice parameter (Å) and N_{Av} is Avogadro's constant.

The densities of all sintered pellets were obtained from their masses and dimensions. These density values were divided by the corresponding theoretical density to obtain the relative densities, ρ_r, of the fired SDC pellets which are presented in Table 6. The highest relative density – 97% of theoretical – was obtained for 10SDC when the highest sintering temperature and the longest sintering time (1450 °C/6 h) were employed. This is consistent with the dilatometry results which showed that sintering of 10SDC was essentially complete at the lowest temperature of the three compositions. In all cases, extension of the sintering time from 4 h to 6 h gave rise only to a very small improvement in density. For all three compositions, relative densities of more than 95% were achieved at sintering temperatures of both 1400 °C and 1450 °C, and times of either 4 h or 6 h. There was also a slight, but general decrease in pellet density with increasing Sm content.

The microstructure of pellets of the three SDC compositions after sintering under the six different sintering regimes was investigated by SEM. Fig. 10 shows SEM images of representative 20SDC samples. In order to quantify differences in microstructure caused by the different sintering regimes, many grains were measured from the SEM images of each pellet type and the resulting data are presented as grain size distribution histograms in Fig. 10. The corresponding figures for the 10SDC and 30SDC compositions are included in the Supplementary Information as Figs. S1 and S2. In
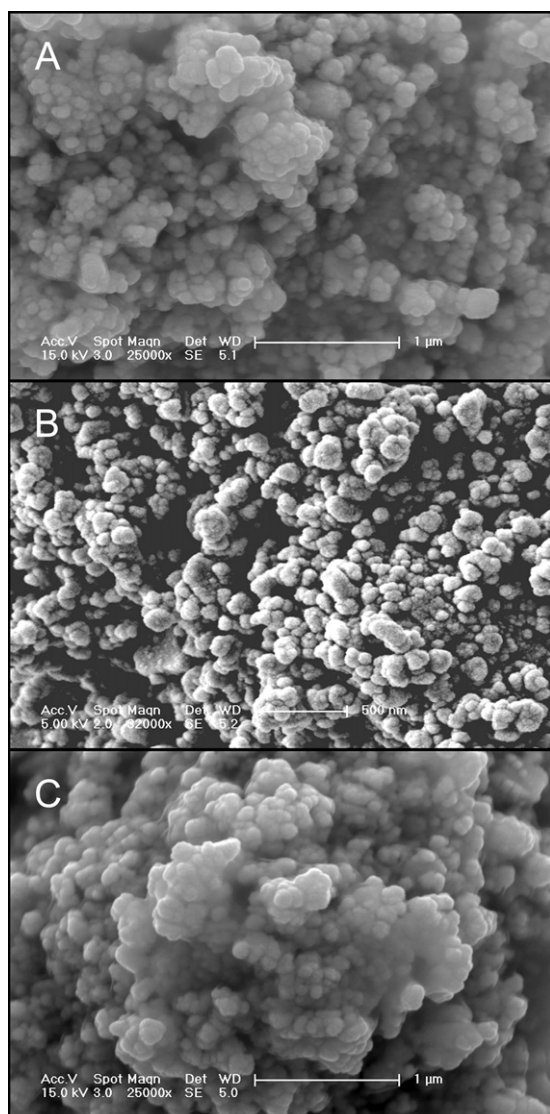
Fig. 6. SEM images of SDC powders calcined at 500 °C for 2 h and milled at 400 rpm for 1 h. (A) 10SDC; (B) 20SDC; (C) 30SDC.

Table 6
Sintering temperature (T_s), sintering time (t_s), relative densities (ρ_r) and average grain size (g_a) of SDC pellets.

Sample	T_s/°C	t_s/h	ρ_r/%	g_a/μm
10SDC			93.1	0.48
20SDC	1300	4	92.1	0.52
30SDC			91.3	0.45
10SDC			96.0	0.75
20SDC	1400	4	95.2	0.81
30SDC			95.0	0.73
10SDC			96.5	0.99
20SDC	1450	4	95.6	1.07
30SDC			95.1	0.91
10SDC			93.7	0.55
20SDC	1300	6	93.0	0.54
30SDC			92.5	0.46
10SDC			96.7	0.77
20SDC	1400	6	95.8	0.88
30SDC			95.3	0.75
10SDC			97.1	1.06
20SDC	1450	6	96.7	1.12
30SDC			96.5	0.94

the SEM images, well-developed, interlocking, roughly hexagonal grains were observed in all samples. Significant porosity was seen in the SDC sample prepared under the mildest sintering regime (1300 °C/4 h) and also, to much lesser extent, in the next-mildest (1400 °C/4 h). The images in Fig. 10(d) and (e), as well as the relative density values in Table 6, indicate that there was a clear reduction in porosity and increase in relative density on sintering at these two temperatures for 2 h longer. The samples sintered at 1400 °C for 6 h and at 1400 °C for 4 h had excellent microstructure, with very low porosity and large grains. Surprisingly, some pores were observed after sintering at the highest temperature for the longer time (1450 °C/6 h, Fig. 10(f)). This phenomenon is known as over-sintering and has been reported to cause a drop in ionic conductivity in $Ce_{0.8}Sm_{0.1}Nd_{0.1}O_{1.9}$ [21]. Grain size distributions for samples sintered at both 4 h and 6 h showed the expected marked increase in mean grain size and broadening of the distribution which would be expected as sintering temperature increased. However, increasing sintering time at the same temperature from 4 h to 6 h had only a small effect on the grain size distributions. Overall, the same trends were seen in the 10SDC and 30SDC samples (Figs. S1 and S2), although porosity was a more marked problem in these two compositions. For example, the 1300 °C/6 h samples both showed significant porosity. However, as for 10SDC, the samples prepared at 1400 °C for 6 h and at 1400 °C for 4 h had very good microstructure. In 10SDC there is some evidence for a bimodal grain size distribution after sintering at 1450 °C, especially for 6 h (Fig. S1). For all compositions, some porosity was observed in the 1450 °C/6 h samples. The effect of Sm content on grain size can most easily be seen in Table 6. In general, 10SDC had the largest mean grain size and 30SDC the smallest. Indeed, 30SDC was found to be the most difficult to sinter as these pellets often cracked during sintering. The data in Table 6 also confirm that changing the sintering time from 4 h to 6 h resulted in only small increases in mean grain size.

3.3. Electrical properties

Conductivity data were calculated from impedance spectra recorded at a number of temperatures from 150 °C to 800 °C in symmetrical cells in flowing dry synthetic air. Under such oxidising conditions, electronic conductivity in SDC and related doped cerias is reported to be very low – giving ionic transport numbers very close to unity – and therefore need not be considered further here [22,23]. Twelve samples were chosen for impedance studies in the light of the results of the density and SEM studies discussed above. Pellets of all three SDC compositions sintered at 1400 °C for 4 h and sintered at 1300 °C, 1400 °C and 1450 °C, each for 6 h, were investigated.

Example impedance spectra (Nquist plots) are presented in Fig. 11 together with the equivalent electronic circuit which was used to fit the impedance data. The spectra are all for pellets of 10SDC and vary only in terms of the sintering regime used to prepare them. All spectra contained two arcs which could be confidently assigned as the bulk and grain boundary responses. Numeric labels indicate the decimal log of the frequency of the applied voltage signal. The bulk arc occurred at the higher frequency. This figure illustrates that changing the sintering regime had very little effect on the bulk arc whereas the grain boundary arc decreased in size (corresponding to a decrease in grain boundary resistance) as the severity of the sintering regime increased from 1300 °C/4 h to 1450 °C/6 h. This is as expected since the grain boundary arc is dependent on the microstructure of the pellet, particularly on the grain size. It has already been shown above that grain size and grain size distribution changed considerably between the different sintering regimes. The spectra in Fig. 11 are consistent with a decrease in grain boundary resistance as mean grain size increased.
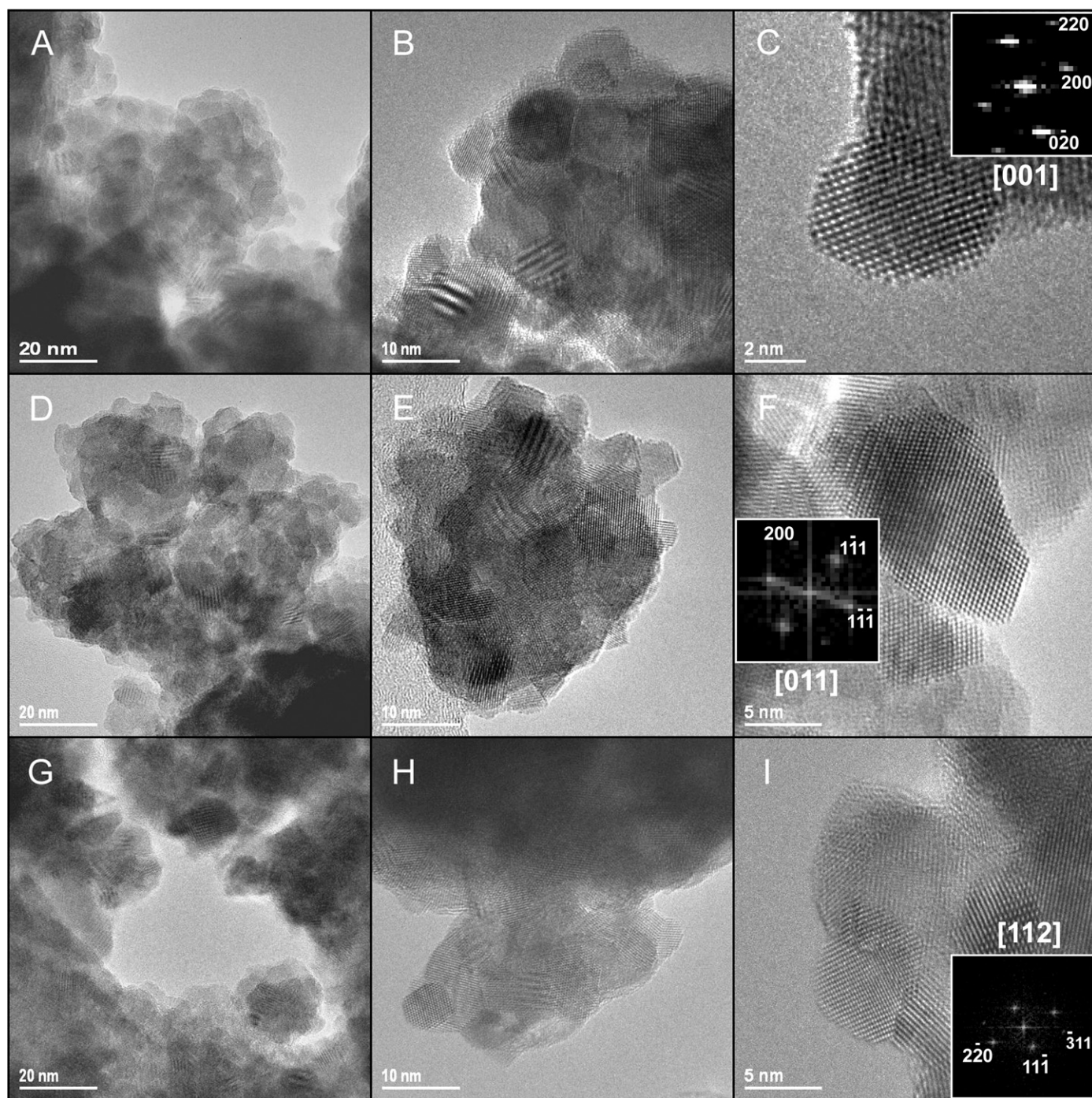
Fig. 7. Low, medium and high magnification TEM images of nanopowders calcined at 500 °C for 2 h. (A, B, C) 10SDC; (D, E, F) 20SDC; (G, H, I) 30SDC. Digital Diffraction Patterns are inset in the high resolution images.

Fig. 12 illustrates the effect of sample composition on the impedance spectra. In this case, all samples were prepared using the same sintering regime: 1400 °C/6 h. In the impedance spectra recorded at 250 °C in Fig. 12(a) and (b) it can be seen that increasing Sm content caused a marked increase in bulk resistance since the corresponding bulk arc increased in size. Overall electrolyte resistance (bulk plus grain boundary) also increased with increasing Sm content. The grain boundary contribution for 30SDC was very small compared to the corresponding bulk arc. In the spectra obtained at 500 °C in Fig. 12(c), the arcs were lost because of a large inductive effect in the apparatus. However, the total electrolyte resistance can be obtained from the intercept of the spectra with the Z' axis.

The electrolyte resistances of 10SDC and 20SDC were very similar at this temperature but 30SDC still had the highest value.

Conductivity values for bulk and grain boundary contributions were calculated from the corresponding resistances obtained by fitting the impedance spectra, the thickness of the SDC electrolyte pellets and the geometric area of the Pt electrodes. Arrhenius-type plots of bulk and grain boundary contributions were constructed using these data and are presented in Fig. 13 for all three SDC compositions and for four sintering regimes. Grain boundary conductivity was found to be higher than bulk conductivity for all compositions. In all cases, bulk conductivity increased with decreasing Sm content, in the temperature range presented in the
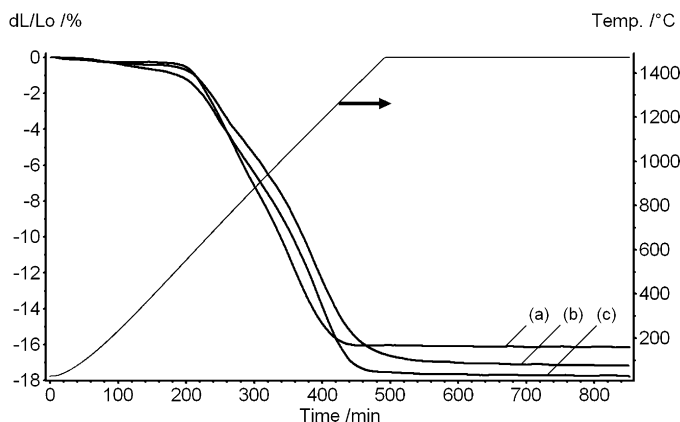
Fig. 8. Linear dilatometry plots of relative length change against time and temperature for compacted nanopowders. (a) 10SDC; (b) 20SDC; (c) 30SDC.

Fig. 9. XRD patterns of SDC pellets after calcination at 1450 °C for 6 h. (a) 10SDC; (b) 20SDC; (c) 30SDC.

figure, and the bulk conductivity of 30SDC was considerably lower than for the other two compositions. However, the traces tend to converge as measurement temperature increased. The individual sintering regime used to prepare the pellets appeared to have little effect on these bulk conductivity plots. This is confirmed in Fig. 14(a) where bulk conductivity measured at 300 °C is plotted against Sm content for the four sintering regimes. For each composition, the data points are closely grouped. However, there does seem to be a trend: bulk conductivity increased with the severity of the sintering regime from 1300 °C/6 to 1400 °C/4 and to 1400 °C/6 but then dropped on going to 1450 °C/6 for all three compositions. Turning to the grain boundary plots in Fig. 13, it is seen that the

Table 7
Activation energies (E_a) of bulk and grain boundary conductivity for SDC pellets prepared following different sintering treatments.

Sample	$T_s/°C$	t_s/h	E_a/eV	
			Bulk	Grain boundary
10SDC			0.72	0.92
20SDC	1300	6	0.90	0.92
30SDC			1.12	1.04
10SDC			0.73	0.91
20SDC	1400	4	0.91	0.97
30SDC			1.13	0.99
10SDC			0.72	0.90
20SDC	1400	6	0.90	1.00
30SDC			1.13	1.04
10SDC			0.72	0.91
20SDC	1450	6	0.91	0.99
30SDC			1.14	1.02

chemical composition of the electrolyte had much less effect than on bulk conductivity. There is a general, small increase in grain boundary conductivity with decreasing Sm content, a trend which mirrors that seen for the bulk conductivity, although it is much less marked. Indeed, in Fig. 13(f) and (g), the traces for 20SDC and 30SDC are essentially coincident. Changing sintering regime had a generally more significant effect on grain boundary than on bulk conductivity as is seen in Fig. 14(b). For each composition, there is a wider spread in the data points than for the bulk data in Fig. 14(a). With the exception of some close and overlapping points, the general trend is of increasing grain boundary conductivity with increasing severity of sintering regime. Grain boundary conductivities were higher than some of those reported in studies of similar compositions prepared by conventional ceramic routes (e.g. [24]). This indicates that the materials obtained in this contribution had low impurity levels.

Apparent activation energies were obtained from the slopes of the Arrhenius-type plots in Fig. 13 and these are presented in Table 7. For bulk conductivity, the activation energies were almost exactly the same for each SDC composition, independent of sintering regime. There were quite large differences between compositions, however. Activation energy increased markedly with increasing Sm content. Turning to the activation energies for the grain boundary conductivity, again there was little change between sintering regimes for each individual composition and there was a small general increase in activation energy with increasing Sm content.

While bulk and grain boundary conductivities give useful insight into the composition–microstructure–conductivity relationship,
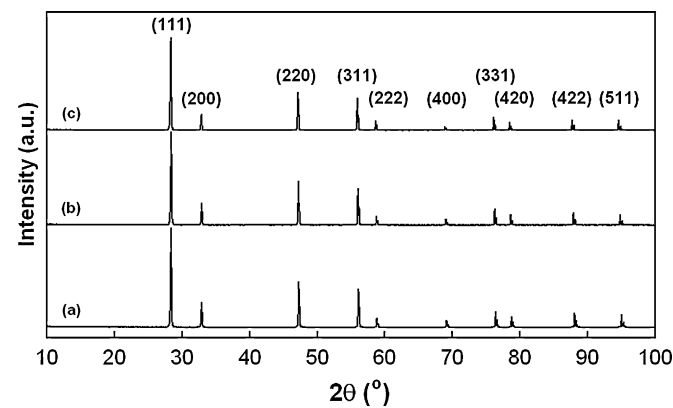
Table 8
Total conductivity data (σ), activation energies (E_a) and association enthalpies (ΔH_a) for SDC pellets prepared following different sintering treatments.

| Sample	$T_s/°C$	t_s/h	$\sigma/\times10^{-2}$ S cm^{-1}			E_a/eV		
			500 °C	600 °C	700 °C	<500 °C	>500 °C	$\Delta H_a/eV$
10SDC			0.64	1.41	2.02	0.76	0.38	0.38
20SDC	1300	6	0.50	1.43	2.20	0.88	0.47	0.41
30SDC			0.20	0.82	1.68	1.12	0.66	0.46
10SDC			0.76	1.60	2.56	0.75	0.42	0.33
20SDC	1400	4	0.59	1.61	2.67	0.91	0.50	0.41
30SDC			0.20	0.89	2.08	1.12	0.73	0.39
10SDC			0.78	1.68	2.69	0.75	0.43	0.32
20SDC	1400	6	0.65	1.73	3.08	0.92	0.49	0.43
30SDC			0.23	0.99	2.27	1.13	0.71	0.42
10SDC			0.74	1.61	2.56	0.74	0.42	0.32
20SDC	1450	6	0.63	1.81	3.07	0.89	0.50	0.39
30SDC			0.24	1.00	2.27	1.13	0.71	0.42
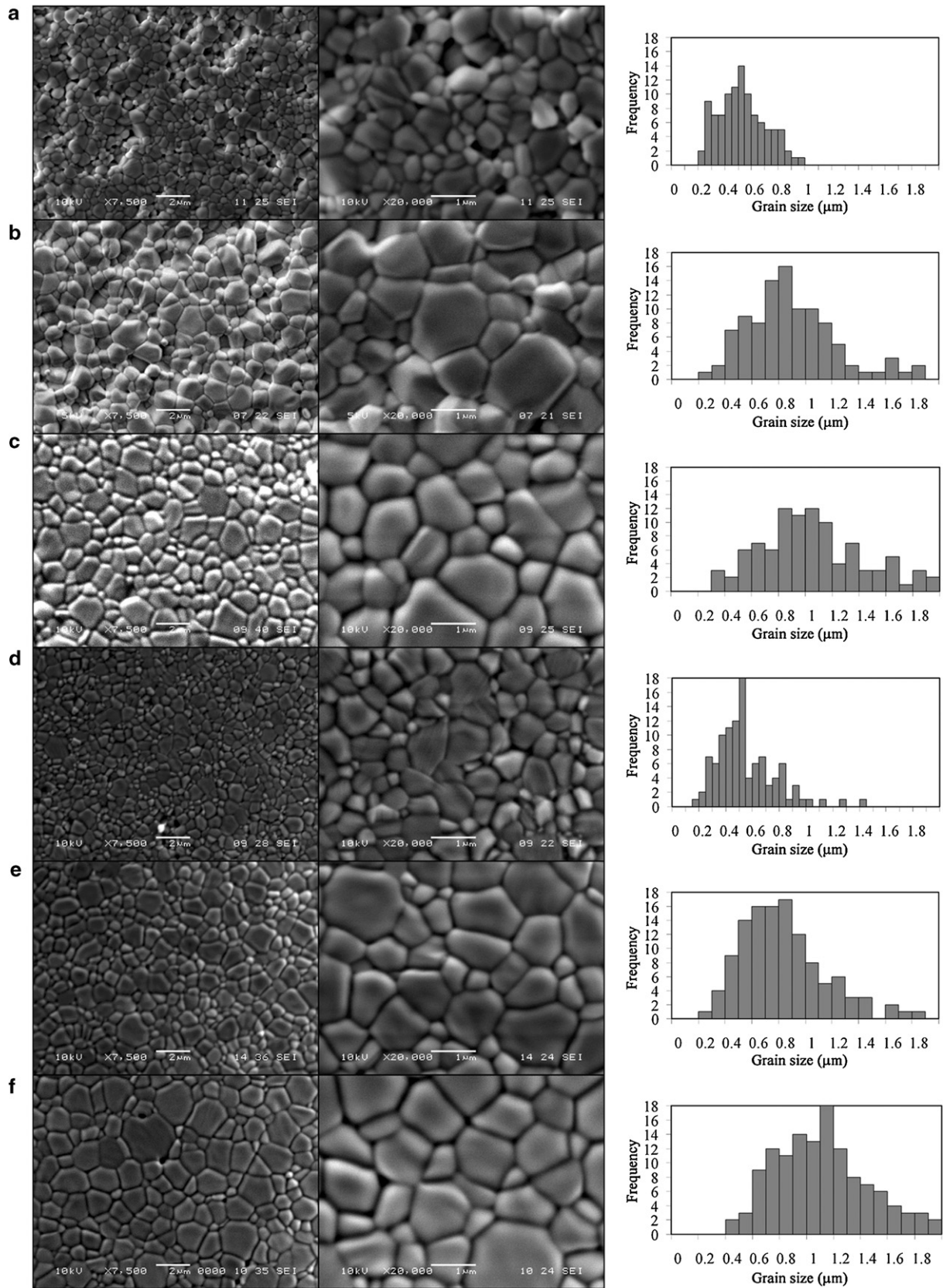
Fig. 10. Low and high magnification SEM images and associated grain size distribution histograms for 20SDC pellets after sintering as follows: (a) 1300 °C/4 h, (b) 1400 °C/4 h, (c) 1450 °C/4 h, (d) 1300 °C/6 h, (e) 1400 °C/6 h and (f) 1450 °C/6 h.
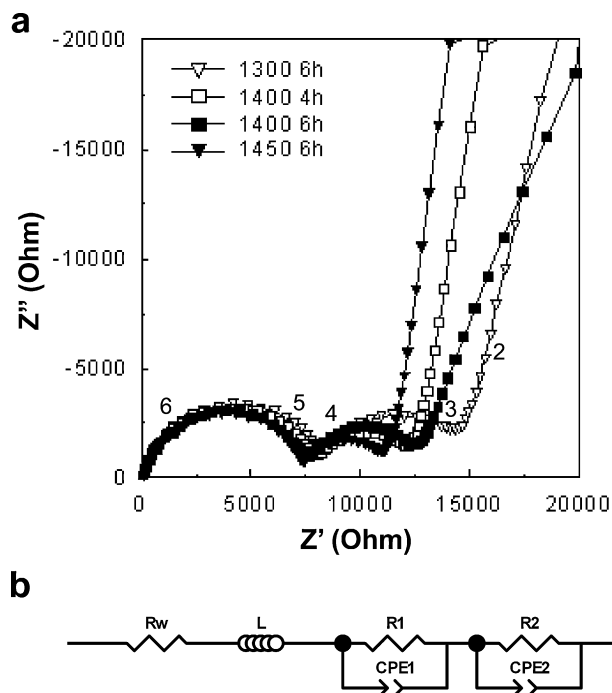
Fig. 11. (a) Impedance spectra of 10SDC pellets prepared under different sintering regimes. Recorded at 200 °C; (b) the corresponding equivalent circuit model.

total electrolyte conductivity is an important parameter for the comparison of electrolyte materials. The total electrolyte conductivity values in this work compared favourably with those quoted in the literature for materials of similar composition [25,26]. To provide a convenient comparison between all SDC samples, the total conductivity data recorded at 500 °C and at 600 °C are presented in Fig. 15. At 500 °C, it is clear that total conductivity increased as Sm content decreased. However, starting at about 600 °C, the 20SDC samples begin to overtake 10SDC to attain the highest total conductivity values. This is clear by 700 °C. These total conductivity values, including those at 700 °C, as well as the activation energies for total conductivity in low and high measurement temperature regions, are summarized in Table 8. There was a clear general increase in total conductivity with increasing sintering time (at the same sintering temperature) and with increasing sintering temperature (for 6 h). This can be attributed to increases in grain boundary conductivity related to an increase in sample density and in grain size as the severity of the sintering regime increased. However, there was an exception to this general trend. Surprisingly, on going from the 1400 °C/6 h regime to the 1450 °C/6 h regime, most of the total conductivity values for 20SDC and 30SDC stayed about the same and those for 10SDC decreased. Since mean grain size and density increased on going from the 1400 °C/6 h regime to the 1450 °C/6 h regime, it seems that these changes in conductivity must be related to some other change in the samples prepared at 1450 °C for 6 h. Indeed the evidence from Fig. 14 is that grain boundary conductivity increased with increasing sintering temperature, while the bulk conductivity showed a drop between 1400 °C/6 h and 1450 °C/6 h. Although this decrease was relatively small, it appeared to dominate the total conductivity because bulk conductivity was significantly lower than grain boundary conductivity in all cases in these materials. Liu et al. observed a similar oversintering effect – re-emergence of pore formation and decrease in total ionic conductivity at high sintering temperatures – in Sm- and Nd-co-doped ceria electrolytes sintered at temperatures from 1400 °C to 1600 °C [21]. Sha et al. prepared electrolyte pellets of $Ce_{0.8}Sm_{0.1}Y_{0.1}O_{1.9}$ by sintering at tempera-
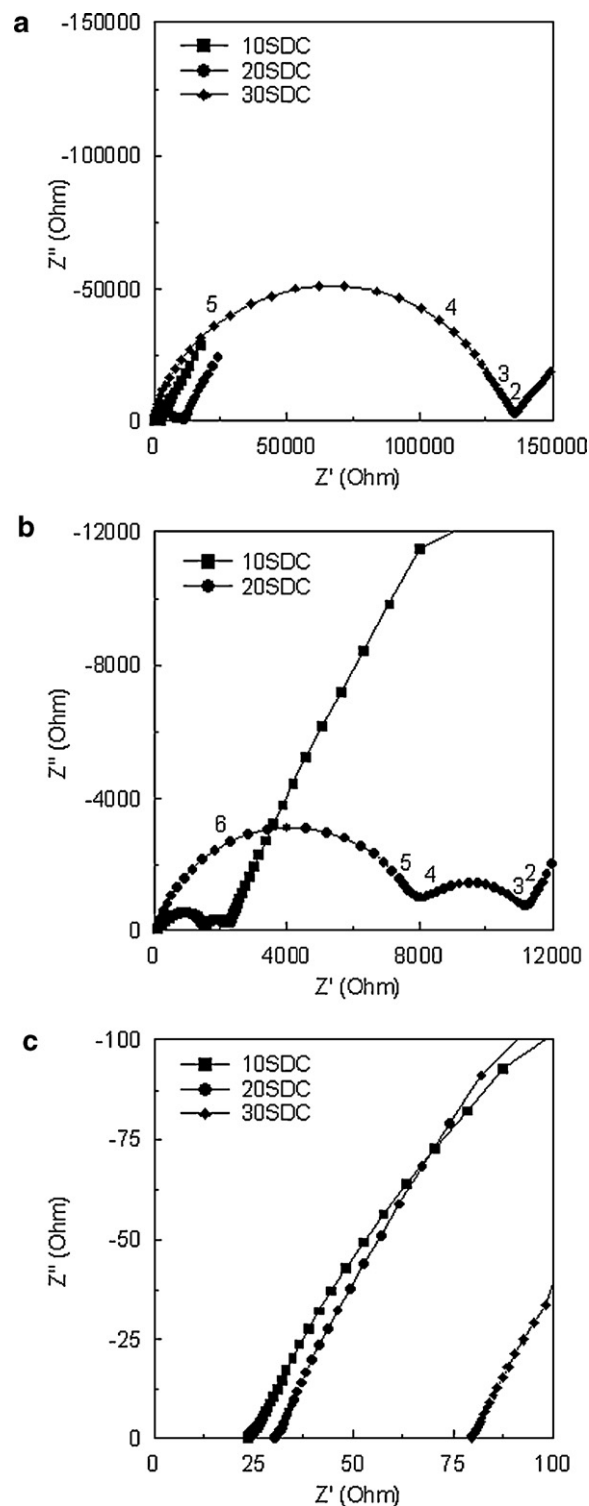

Fig. 12. Impedance spectra of SDC pellets sintered at 1400 °C for 6 h. (a) Recorded at 250 °C; (b) recorded at 250 °C, detail showing spectra for 10SDC and 20SDC; (c) recorded at 500 °C.

tures of 1300–1600 °C [27]. They obtained total, bulk and grain boundary conductivity values at measurement temperatures from 300 °C to 600 °C and observed a decrease in total conductivity with increasing sintering temperature which also coincided with the emergence of porosity in the samples. Grain boundary conductivity decreased as sintering temperature was increased from 1300 °C to 1500 °C, but then remained approximately constant on going from
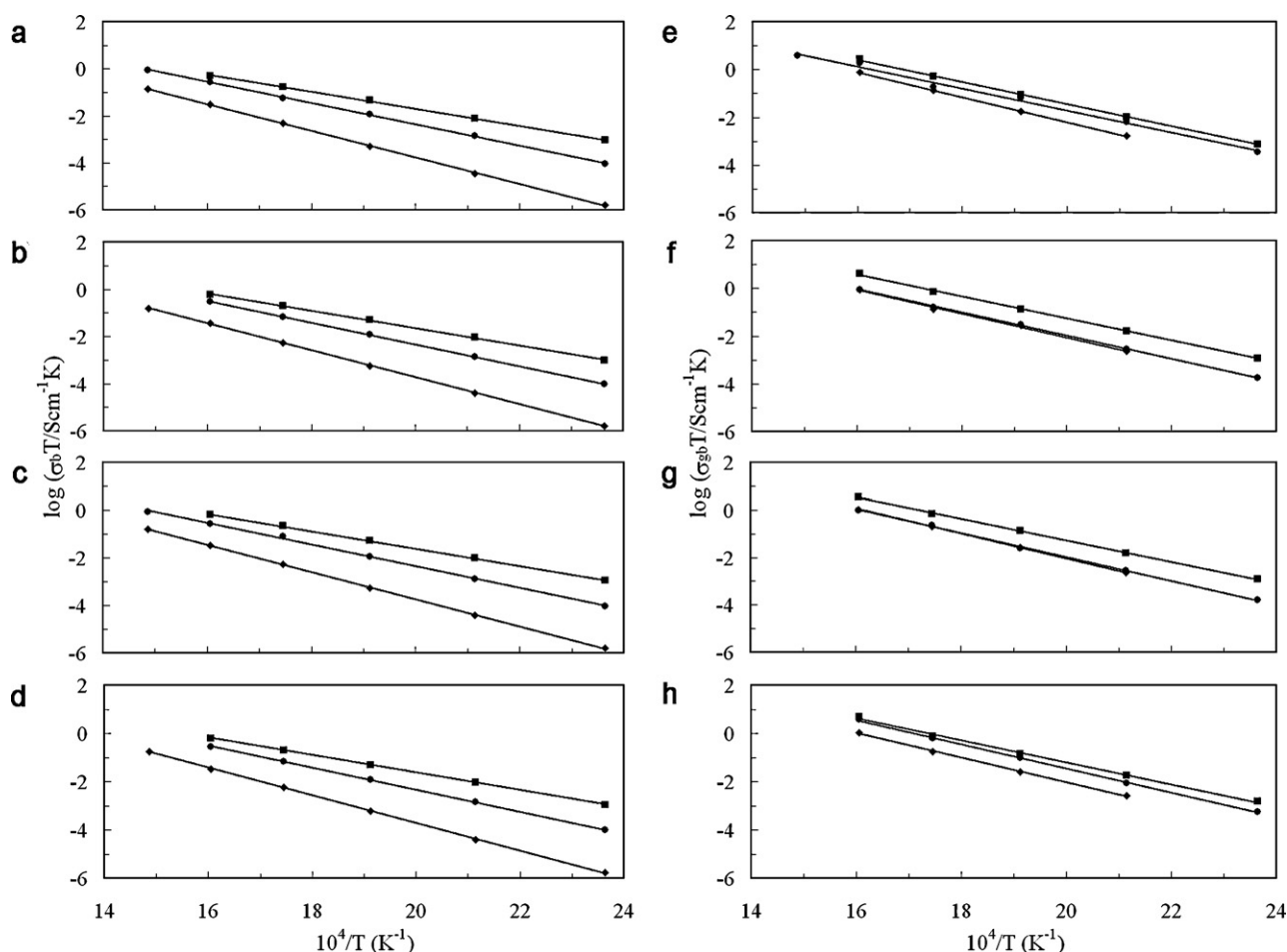
Fig. 13. Arrhenius-type plots of (a–d) bulk and (e–h) grain boundary conductivity of (■) 10SDC, (●) 20SDC and (♦) 30SDC samples sintered at (a,e) 1300 °C/6 h; (b,f) 1400 °C/4 h; (c,g) 1400 °C/6 h; (d,h) 1450 °C/6 h.

1500 °C to 1600 °C. Bulk conductivity, however, showed clear general decreases from 1400 °C to 1500 °C and from 1500 °C to 1600 °C. Therefore, it appears that oversintering caused changes which had (at least partly) independent effects on grain boundary and on bulk conductivity. The changes in grain boundary conductivity can be explained by the competing effects of increasing grain size and increasing porosity. The decrease in bulk conductivity would normally be expected to be caused by a chemical or phase change within the bulk material, although no evidence for the latter is seen in the accompanying XRD patterns. In the SDC samples of the current contribution, a similar decrease in bulk conductivity accompanied by emergence of porosity at the highest sintering temperature was observed, most markedly for 10SDC. It is not possible to attribute this effect definitively. The only process which might affect bulk conductivity without affecting the XRD patterns noticeably would be low level diffusion of Sm ions within the individual grains of the material, giving rise to small domains with slightly differing Sm concentrations – and therefore differing conductivities – but retaining the original crystal structure. However, detailed high temperature studies would be required to investigate this possibility further.

The activation energies of total conductivity are presented in Table 8 for the temperature regions below 500 °C and above 500 °C. This is because there was a clear change of gradient at around this temperature. This can be seen for all SDC compositions after the same sintering regime in Fig. 16 and was found to be a completely general effect across all samples studied. In Table 8 it is clear that the effect of sintering regime on these values was again minimal: nei-

ther the values above nor those below 500 °C changed significantly between different sintering regimes for the same SDC composition. However, as was seen for the bulk and grain boundary activation energies, SDC composition had a strong effect on activation energy, which increased with increasing Sm content in all cases. For all SDC compositions and all sintering regimes, the activation energies of total conductivity at measurement temperatures above 500 °C were significantly smaller than those pertaining below 500 °C. The difference ranged from 0.32 eV to 0.46 eV and showed a tendency to increase with increasing Sm content, particularly from 10SDC to 20SDC. Qualitatively similar effects have been reported for similar materials. Zhan et al. observed a curvature in Arrhenius-type conductivity plots for a range of SDC samples prepared by solid state reaction [24]. Arachi et al. reported similar behaviour for YSZ and Scandia Stabilised Zirconia systems and explained it as an effect related to the dissociation energy required to separate an oxide ion vacancy from a dopant ion site [1]. Piñol et al. observed a distinct slope change at 700 °C for GDC and suggested that this was caused by increasing interactions between the dopant species and the charge carriers with decreasing temperature [28]. Steele discussed such a change in the activation energy of conductivity in GDC in terms of the migration enthalpy of oxygen ion vacancies, ΔH_m, and the association enthalpy, ΔH_a, between Gd sites and oxygen ion vacancies, Gd'_{Ce}-$V_o^{\bullet\bullet}$, which must be overcome to free vacancies so that they may become involved in conduction [25]. In high purity $Ce_{0.9}Gd_{0.1}O_{1.9}$, Steele obtained values of $\Delta H_m = 0.64$ eV and $\Delta H_a = 0.13$ eV with an inflection in the Arrhenius-type conductivity plot at around 400 °C. In the current contribution, we can equate
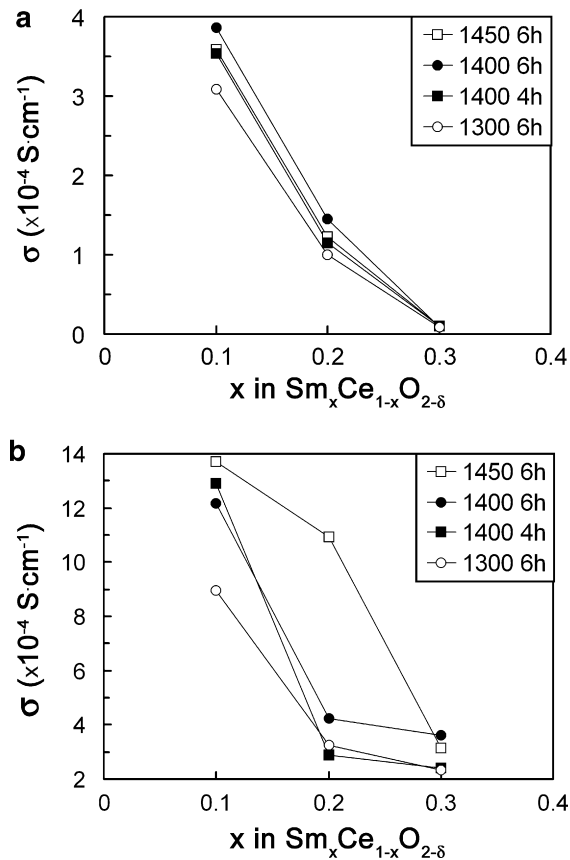
Fig. 14. (a) bulk and (b) grain boundary conductivity measured at 300 °C for SDC pellets prepared following different sintering treatments as a function of Sm content.

Fig. 15. Total conductivity of SDC pellets prepared following different sintering treatments as a function of Sm content. Measured at (a) 500 °C; (b) 600 °C.

the activation energy of the electrolyte contribution at temperatures above 500 °C to the migration enthalpy, with average values of $\Delta H_m = 0.41$ eV for 10SDC, 0.49 eV for 20SDC and 0.70 eV for 30SDC. If we assume the difference between the activation energies in the high and low temperature regimes equates to the association enthalpy of Sm'_{Ce}-$V_o^{\bullet\bullet}$ species, [12] we obtain average values of $\Delta H_a = 0.34$ eV for 10SDC, 0.41 eV for 20SDC and 0.42 eV for 30SDC. Clearly, ΔH_m was the more sensitive of these two enthalpies to Sm content and was particularly high for 30SDC.

The activation energies below 500 °C for total electrolyte conductivity (Table 8) match very closely with those for bulk conductivity but not with those for grain boundary conductivity (Table 7). This indicates that the bulk contribution was dominant over the grain boundary contribution in these materials. This is in agreement with the data of Fig. 13, in which bulk conductivity was lower in all cases than grain boundary conductivity. In addition, the activation energies for grain boundary contribution are in the range 0.90–1.04 eV, and so are broadly in the same range as the values for bulk conductivity. Both these factors indicate that the change in gradient in the Arrhenius-type plot (Fig. 16) is not due to a dominant grain boundary effect in the low temperature region, since grain boundary conductivities would have to be lower and the activation energies for grain boundary conductivity would have to be significantly higher than those for bulk conductivity. This allows some confidence in the values attributed to ΔH_m and ΔH_a.

The work of Faber et al. [29] is relevant to the increase in ΔH_m observed with increasing Sm content. These authors studied the oxygen ion conductivities of ceria doped with Nd, La, Gd, Y and Yb. They extracted overall activation energies – i.e. $\Delta H_a + \Delta H_m$ – and found a general trend for all dopants: activation energies fell to a minimum at dopant concentrations of around 2–5 mol%
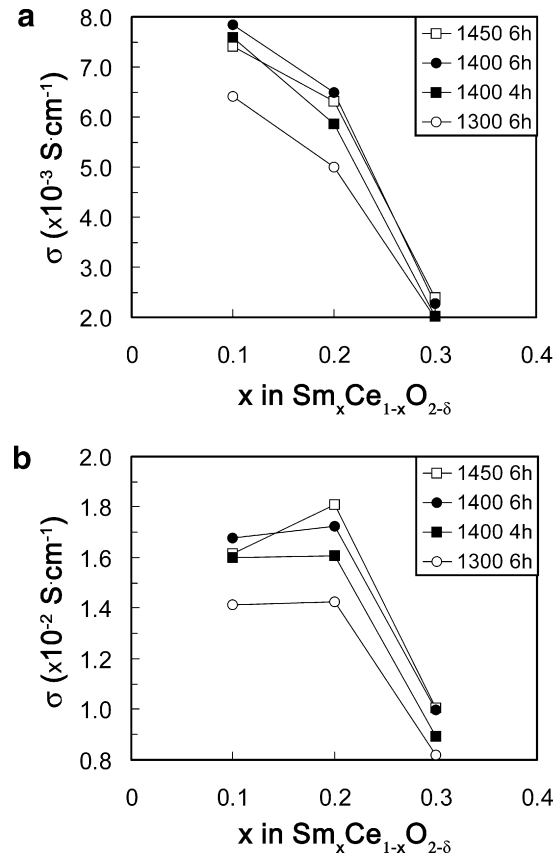
and then increased sharply on going to higher dopant concentrations. The authors also cite a value of $\Delta H_m = 0.49$ eV obtained for lightly Y-doped CeO_2 from an earlier ^{17}O NMR study [30]. More specifically, in a recent paper, [31] Omar et al. obtained activation energy values for bulk ionic conductivity in $Sm_{x/2}Nd_{x/2}O_{2-\delta}$ ($x = 0$–0.18) at temperatures above and below 475 °C. Applying the procedure described above, they obtained values for ΔH_m which showed a minimum at a dopant concentration of about 5 mol% but then increased with increasing dopant concentration. They
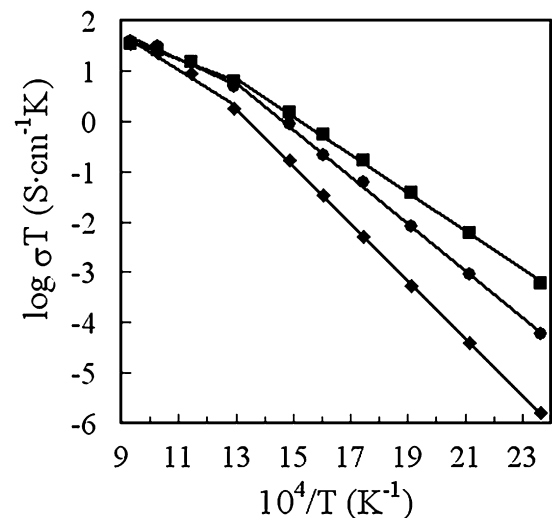

Fig. 16. Arrhenius-type plots of total electrolyte conductivity of (■) 10SDC, (●) 20SDC and (♦) 30SDC. Samples sintered at 1400 °C for 6 h.

obtained $\Delta H_m = 0.65$ eV for $x = 0.10$ and $\Delta H_m = 0.80$ eV for $x = 0.18$, the highest value used. A similar increase in ΔH_m with increasing Sm dopant content was observed in the SDC samples described in the present contribution, although the actual values were significantly lower than for the Nd and Sm co-doped materials. This may be related to the different chemical environments – with or without Nd – of the oxygen ions and the oxygen vacancies in these two sets of materials.

Turning to the values of ΔH_a, the association enthalpy of Sm'_{Ce}-$V_o^{\bullet\bullet}$ species, Omar et al. [31] obtained a very low and approximately constant value of $\Delta H_a \sim 0.05$ eV for $Sm_{x/2}Nd_{x/2}O_{2-\delta}$ in the range, $x = 0.08$–0.18. Kilner [12] reviewed ΔH_a data for CeO_2 doped with trivalent cations, although not Sm^{3+}. However, Gd^{3+} is only slightly smaller (107.8 pm) than Sm^{3+} (109.8 pm) and Kilner did refer to calculated and experimental ΔH_a values of 0.13 eV and 0.17 eV, respectively, for GDC. The former matches the value given by Steele, also for GDC [25]. These values are considerably lower than those obtained for SDC in the present study. However, this review also cited the calculations of Minervini et al. [32] who did not consider Sm but gave a value of about 0.38 eV for GDC in which the oxygen vacancy, $V_o^{\bullet\bullet}$, is either a nearest or next nearest neighbour to the Gd'_{Ce} species (ΔH_a falls to 0.21 eV if the $V_o^{\bullet\bullet}$ is a third nearest neighbour). Also, Faber et al. [29] obtained ΔH_a values by extrapolating their data to infinite dopant dilution for a number of dopants, assuming $\Delta H_m = 0.5$ eV (see above). They obtained $\Delta H_a = 0.23$ eV, 0.29 eV, 0.32 eV, 0.40 eV and 0.67 eV for Nd, La, Gd, Y and Yb dopants, respectively. These last calculated and experimental values for GDC are close to that obtained in the present study, $\Delta H_a = 0.38$ eV, for the sample with the closest dopant concentration, 10SDC.

It is clear that poorly conducting grain boundaries would strongly affect plots of total conductivity and may therefore cause inaccuracies in ΔH_a and ΔH_m values obtained from them. However, this does not seem to apply to the present work since the grain boundary conductivity, unusually, was always higher than that of the bulk. This appears to be a consequence of reducing the incorporation of impurities by using nitrate precursors in the low temperature citrate synthesis route rather than a high temperature ceramic route from the simple oxides, for example.

It is interesting to speculate on the possible effects of preparation route on the mechanisms of ion migration and defect trapping. For example, ideally, the citrate route gives rise to atomic mixing of the dopant (Sm) and host (Ce) cations. The ceramic route relies on inter-diffusion of the starting oxides at high temperature to form the product. Under certain circumstances, this may lead to a product containing nanodomains, too small to detect by XRD, but with differing dopant concentrations. It would be interesting to model such a heterogeneous structure to study how the phenomena of oxygen ion migration, oxygen vacancy trapping and the formation of clusters of more than two defects, and, therefore, ΔH_a and ΔH_m, would be affected.

4. Conclusions

A compositional series of high purity, nanoparticulate SDC materials was successfully prepared by a low temperature, inexpensive citrate complexation method. Crystallization of the SDC product occurred via three exothermic processes and the final crystal structure first formed from the gel at a temperature below 300 °C. After calcination at 500 °C, electron microscopy and XRD revealed that the products were foam-like, single-phase materials with high porosity and consisted of primary crystalline particles of about 10 nm diameter present in small clusters. These materials were milled and the resulting nanopowders were used in a detailed study of the effect of chemical composition, sintering temperature and sintering time on their densification, and on the grain struc-

ture and ionic conductivity of the resulting dense pellets. Densities of over 95% of theoretical were achieved for all three compositions after sintering at 1400 °C or higher for 4 h or longer and both density and average grain size increased with increasing sintering temperature and sintering time, although the effect of the former was much more marked. Samples sintered at 1400 °C for 6 h or 1450 °C for 4 h showed excellent microstructure for all compositions. However, some porosity was observed after sintering at 1450 °C for 6 h and this oversintering had a deleterious effect on the overall conductivity, especially of the 10SDC. Arrhenius-type plots of electrolyte conductivity showed an inflexion at around 500 °C and this was interpreted in terms of a defect association enthalpy, ΔH_a, and an oxygen migration enthalpy, ΔH_m, both having been important at low temperatures while the latter became dominant at high temperatures. ΔH_a was less sensitive to Sm content and had values of around 0.4 eV. ΔH_m increased significantly with %Sm and had values of 0.4–0.7 eV. At 600 °C, the highest total conductivity was 1.81×10^{-2} S cm^{-1} for the 20SDC sample sintered at 1450 °C for 6 h.

Acknowledgements

Appendix A. Supplementary data

Supplementary data associated with this article can be found, in the online version, at doi:10.1016/j.jpowsour.2010.11.041.

References

[1] Y. Arachi, H. Sakai, O. Yamamoto, Y. Takeda, N. Imanishai, Solid State Ionics 121 (1999) 133–139.
[2] C. Peng, Y.N. Liu, Y.X. Zheng, Materials Chemistry and Physics 83 (2003) 509–514.
[3] S. Zha, C. Xia, G. Meng, Journal of Power Sources 115 (2003) 44–48.
[4] M.G. Bellino, D.G. Lamas, N.E. Walsöe de Reca, Advanced Functional Materials 16 (2006) 107–113.
[5] J.B. Wang, W.-H. Shih, T.-J. Huang, Applied Catalysis A: General 203 (2000) 191–199.
[6] C. Pijolat, G. Tournier, J.P. Viricelle, Sensors and Actuators B: Chemical 141 (2009) 7–12.
[7] J.-Y. Park, E.D. Wachsman, Journal of The Electrochemical Society 152 (2005) A1654–A1659.
[8] C. Lu, S. An, W.L. Worrell, J.M. Vohs, R.J. Gorte, Solid State Ionics 175 (2004) 47–50.
[9] S. Zhao, R.J. Gorte, Applied Catalysis A: General 277 (2004) 129–136.
[10] S. Song, R.O. Fuentes, R.T. Baker, Journal of Materials Chemistry (2010), doi:10.1039/C0JM01741H.
[11] M. Mogensen, D. Lybye, N. Bonanos, P.V. Hendriksen, F.W. Poulsen, Solid State Ionics 174 (2004) 279–286.
[12] J.A. Kilner, Solid State Ionics 129 (2000) 13–23.
[13] Y. Wang, T. Mori, J.-G. Li, Y. Yajima, Science and Technology of Advanced Materials 4 (2003) 229.
[14] J.P. Hos, P.G. McCormick, Scripta Materialia 48 (2003) 85–90.
[15] R.D. Purohit, S. Saha, A.K. Tyagi, Ceramics International 32 (2006) 143–146.
[16] Y.-P. Fu, C.-H. Lin, C.-W. Liu, K.-W. Tay, S.-B. Wen, Journal of Power Sources 159 (2006) 38–41.
[17] R.O. Fuentes, R.T. Baker, Journal of Power Sources 186 (2009) 268–277.
[18] R.O. Fuentes, R.T. Baker, International Journal of Hydrogen Energy 33 (2008) 3480–3484.
[19] J. Rodríguez-Carvajal, FullProf98, Version 0.2, Laboratoire León Brillouin (CEA-CNRS), Saclay, France, 1998.
[20] M.M. Barbooti, D.A. Alsammerrai, Thermochimica Acta 08 (1986) 119–126.
[21] Y. Liu, B. Li, X. Wei, W. Pan, Journal of the American Ceramic Society 91 (2008) 3926–3930.
[22] J.C.C. Abrantes, D. Pérez-Coll, P. Núñez, J.R. Frade, Electrochimica Acta 48 (2003) 2761–2766.
[23] T. Shimonosono, Y. Hirata, Y. Ehira, S. Sameshima, T. Horita, H. Yokokawa, Solid State Ionics 174 (2004) 27–33.
[24] Z. Zhan, T.-L. Wen, H. Tu, Z.-Y. Lu, Journal of the Electrochemical Society 148 (2001) A427–A432.
[25] B.C.H. Steele, Solid State Ionics 129 (2000) 95–110.

[26] V.V. Kharton, F.M.B. Marques, A. Atkinson, Solid State Ionics 174 (2004) 135–149.
[27] X. Sha, Z. Lu, X. Huang, J. Miao, Z. Liu, X. xin, Y. Zhang, W. Su, Journal of Alloys and Compounds 433 (2007) 274–278.
[28] S. Piñol, M. Najib, D.M. Bastidas, A. Calleja, X.G. Capdevila, M. Segarra, F. Espiell, J.C. Ruiz-Morales, D. Marrero-López, P. Nuñez, Journal of Solid State Electrochemistry 8 (2004) 650–654.
[29] J. Faber, C. Geoffroy, A. Roux, A. Sylvestre, P. Abelard, Applied Physics A 49 (1989) 225–232.
[30] K. Fuda, K. Kishio, S. Yamauchi, K. Fucki, Y. Onoda, Journal of Physics and Chemistry of Solids 45 (1984) 1253–1257.
[31] S. Omar, E.D. Wachsman, J.C. Nino, Solid State Ionics 178 (2008) 1890–1897.
[32] L. Minervini, M.O. Zacate, R.W. Grimes, Solid State Ionics 116 (1999) 339–349.